nature energy

Article

https://doi.org/10.1038/s41560-026-02010-z

Additive-assisted perovskite crystallization on industrial TOPCon silicon for tandem solar cells with improved efficiency

Received: 17 April 2025

Accepted: 18 February 2026

Qilin Zhou[1,2,13], Renjun Guo[2,13], Shunchang Liu[1,2,3,13], Nengxu Li[1,2,13], Menglei Xu[4,5,13], Xinyu Zhang[4,5,6] ✉, Xianyuan Jiang[7], Lu Wang[8], Laura-Isabelle Dion-Bertrand[9], Zhuojie Shi[1,2], Xiao Guo[1,2], Haoming Liang[1,2], Zijing Dong[1,2], Jinxi Chen[1,2], Yu-Duan Wang[1,2], Ran Luo[1,2], Xi Wang[1,2], Jungan Wang[4,5], Jie Yang[4], Hao Jin[6], Chun-Hsiao Kuan[10,11], Sung-Fu Hung[10,11], Zhenrong Jia[1,2], Ling Kai Lee[2], Donny Lai[2], Eric Wei-Guang Diau[10,11], Wentao Yan[12] & Yi Hou[1,2] ✉

Thin silicon wafers used in tunnel oxide passivated contact tandem solar cells have reduced thermal mass and higher thermal conductivity, which accelerate heat transfer during perovskite subcell deposition. This rapid heat transfer induces fast crystallization of the perovskite layer, compromising film quality and tandem performance. Here we introduce 2-mercaptobenzothiazole, which exhibits dual-mode binding with perovskite organic cations, to modulate crystallization dynamics. This approach improves morphological uniformity, eliminates voids and suppresses halide segregation, while reducing non-radiative recombination and lowering the trap-assisted recombination rate from 3.2×10^5 to 4.3×10^4 cm s^{-1}. The two-terminal monolithic perovskite/tunnel oxide passivated contact tandem cell achieves a certified stabilized power conversion efficiency of 32.76% and retains 91% of its initial efficiency after 1,700 h of continuous operation. This work uncovers a previously overlooked perovskite crystallization issue on industrial silicon wafers, providing critical insights for integrating perovskite solar cells into mainstream silicon technology.

Crystalline silicon (c-Si) photovoltaics have long dominated the global photovoltaic market, holding a 97% market share as of 2024[1]. The industry's transition from passivated emitter and rear cell (PERC) designs to more advanced tunnel oxide passivated contact (TOPCon) solar cells has progressed much more rapidly than anticipated[2]. Today, TOPCon technology has become the most widely deployed photovoltaic solution, offering superior surface passivation that leads to higher efficiency, a lower temperature coefficient and compatibility with existing PERC production lines. Its excellent passivation quality also ensures consistent performance even with thinner wafers, making it a leading choice in the current photovoltaic market[3–5].

The mainstream adoption of silicon technology will influence the choice of silicon bottom cells in perovskite/Si tandems. Recent efficiency improvements in c-Si photovoltaics have been driven by advances in passivating contact technologies, including silicon heterojunction (SHJ), TOPCon solar cells and back contact (BC) solar cells[6–8]. In 2024, TOPCon technology achieved a power conversion efficiency (PCE) of 26.58%, narrowing the efficiency gap with SHJ to less than 1% (ref. 9). This makes further expansion of the SHJ market increasingly challenging. Whereas BC solar cells show potential as the next major silicon single-junction technology after TOPCon, they are not ideal for integration into monolithic tandem modules with perovskites[10].

A full list of affiliations appears at the end of the paper. ✉e-mail: xinyu.zhang@jinkosolar.com; yi.hou@nus.edu.sg

The photovoltaic market is likely to remain TOPCon-dominated in the near term. At present, reported perovskite/SHJ tandem devices lead with proof-of-concept certified efficiency of 34.58% (refs. 11–14), whereas the reported perovskite/TOPCon tandems have only reached a certified 32.32% efficiency in the literature so far[15–20].

The dominance of c-Si photovoltaics in the market is driven by continuous innovations that improve efficiency while reducing costs[21,22]. In terms of cost, the industry has substantially decreased Si wafer thickness from 300 μm in 2004 to the current industrial standard of 130 μm (refs. 1,21). However, this shift presents a major challenge: depositing high-quality perovskite films on these industrially fabricated thin Si wafers.

Although perovskite crystallization has been thoroughly explored in single-junction[23] and multi-junction[24–26] perovskite solar cells fabricated on standard glass substrates, transitioning perovskite processing from glass to tandem architectures using Si wafers introduces a set of challenges that the community has not yet fully addressed. A key factor is the thermal conductivity of the substrate itself—a critical but often overlooked component[27]. Unlike glass, silicon substrates have higher thermal conductivity and, when thinner, can accelerate heat transfer during the perovskite annealing process. This rapid heat dissipation can result in uncontrolled crystallization, leading to defects and poor morphology in the perovskite films. Developing a tailored approach to perovskite crystallization dynamics, specifically designed for integrating high-quality perovskite layers with industrially fabricated thin TOPCon bottom cell, remains a critical gap. Addressing this challenge would enable a more transformative and commercially viable solution for perovskite/Si tandems. Studies of perovskite crystallization issues when using thin silicon wafers as the substrates are lacking, making our study one of the earliest to highlight and investigate this effect.

In this Article, we investigate the heat transfer profile and its impact on perovskite crystallization when growing perovskite on industrial Si substrates in one-step solution processed perovskite for two-terminal perovskite-Si tandem solar cells. We find that the perovskite crystallization rate accelerates by a factor of three on Si substrates compared with typical glass substrates, inducing defective film morphology and optoelectronic properties. To address this, we introduce a dual-mode-binding ligand that controls the principal organic cations (Formamidinium, FA) to regulate crystallization. This approach supplements previous strategies mainly focused on strong coordination with inorganic lead halides[28–31], allowing for refined crystal growth and improved film quality of perovskite films on Si wafers. We achieve an implied open-circuit voltage (iV_{OC}) of 1.29 V for 1.68 eV wide-bandgap perovskite cell, facilitating the successful integration of high-quality wide-bandgap perovskites with industrial Si wafers. This integration results in a power conversion efficiency of 32.54% and stabilized efficiency of 32.76%, both certified by National Photovoltaic Industry Metrology Test Center (NPVM) and an open-circuit voltage (V_{OC}) of 1.97 V for perovskite/TOPCon tandem solar cells. This work not only advances the understanding of substrate-specific perovskite crystallization behaviour but also establishes a suitable pathway to integrate perovskite materials with mainstream silicon technology.

Heat transfer and its impact on perovskite crystallization

First, we employ thermal conduction simulations to investigate how heat transfer influences the crystallization dynamics of perovskite. In Fig. 1a, we compare two distinct substrates: an indium tin oxide (ITO)-glass substrate with a typical thickness of 1.1 mm and an industrial-thin Czochralski (CZ) c-Si wafer with a thickness of 130 μm. The thermal conductivity of c-Si and glass is set to be 148 W mK^{-1} and 0.98 W mK^{-1}, respectively[32]. Notably, the c-Si wafer is approximately ten times thinner than the glass substrate, while its thermal conductivity is approximately 151 times higher than that of the glass, resulting in vastly different heat transfer characteristics. Hence we apply thermal conduction simulations to disclose the different heat transfer behaviours between Si and glass (Fig. 1b and Supplementary Figs. 1 and 2). The curves represent the temperature profiles of the two substrates when placed on a hotplate maintained at 100 °C. The c-Si wafer reaches the target temperature within just 10 seconds, whereas the glass substrate requires over 40 seconds to achieve the same temperature. This discrepancy is especially pronounced during the early stages of heating (Fig. 1c). For instance, at the 5th second, the surface temperature of the c-Si wafer has reached 98 °C, while the glass substrate has only risen to 65 °C (Supplementary Fig. 3). These early-stage heat transfer is crucial for modulating perovskite crystal nucleation and growth and ultimately determining the quality of the resulting perovskite films[27,33].

This huge difference of heat transfer process inspires us to study the crystallization behaviours of perovskite on different substrates. Using in situ photoluminescence (PL) tracking, we observe the distinct crystallization dynamics of perovskite films grown on glass and Si substrates, respectively (Fig. 1d,e and Supplementary Fig. 4a,b). On glass, the PL emission peak gradually shifts from 702.9 nm to 728.3 nm, reflecting an evolving bandgap during the crystallization process. This peak shifting correlates with the formation of bromide-rich nuclei, followed by gradual iodide incorporation into the perovskite lattice during early growth stages[34]. This transition lasts for over 15 seconds on glass, whereas it completes in just 5 seconds on Si, highlighting a markedly threefold accelerated crystallization process. Cross-section scanning electron microscopy (SEM) analysis visually elucidates the impact of crystallization differences on film morphology (Fig. 1f,g). The perovskite film form on glass exhibits a compact and uniform structure, while that on Si displays marked voids close to the buried interface, a feature known to adversely affect device performance[35]. These findings underscore the critical influence of substrate thermal conduction profiles on the crystallization behaviour and resulting film quality of perovskite materials. We decouple the roles accelerated-heat-transfer plays in the formation of voids, and defects, by comparing the perovskite films grown on a Si substrate and thermally retarded Si substrate (Si/Glass, which is a Si wafer fixed on a glass substrate using tape), where we find that if heat transfer is retarded on Si/Glass, the voids are mostly eliminated (Supplementary Fig. 4c,d).

To this point, we have explained why directly adapting perovskite recipes optimized for standard glass-based devices to tandem cells is fundamentally ineffective. The primary challenge arises from the rapid crystallization induced by high thermal conductivity and reduced thickness of industrial Si substrates, which disrupts the formation of high-quality perovskite films. Figure 1h schematically illustrates the relationship between the crystallization dynamics and resulting perovskite morphologies on glass and Si substrates, respectively. During annealing, perovskite films crystallize in a top-down manner, thus the residual solvent is trapped at bottom region and escaped through unsolidified pathways in the upper perovskite layer[36,37]. On glass, the slower temperature ramp allows sufficient time for solvent evaporation, leading to compact, pinhole-free films. In contrast, the ultra-fast heat transfer on Si prematurely solidifies the upper perovskite layer, trapping residual solvent underneath. This results in void formation and defective morphologies within the films.

Refining crystallization by dual-mode binding ligand for FA$^+$

The rapid and poorly controlled perovskite crystallization dynamics on thin Si wafers pose a critical challenge for achieving high-performance perovskite-Si tandem cells. To address this, we carefully examine the composition of perovskite precursor, which includes both inorganic components (for example, lead halides) and organic counterparts (for example, formamidinium iodide and methylammonium bromide). Although the addition of dimethyl sulfoxide (DMSO) has been shown to moderate perovskite crystallization through strong interactions with inorganic lead halides and the minority organic

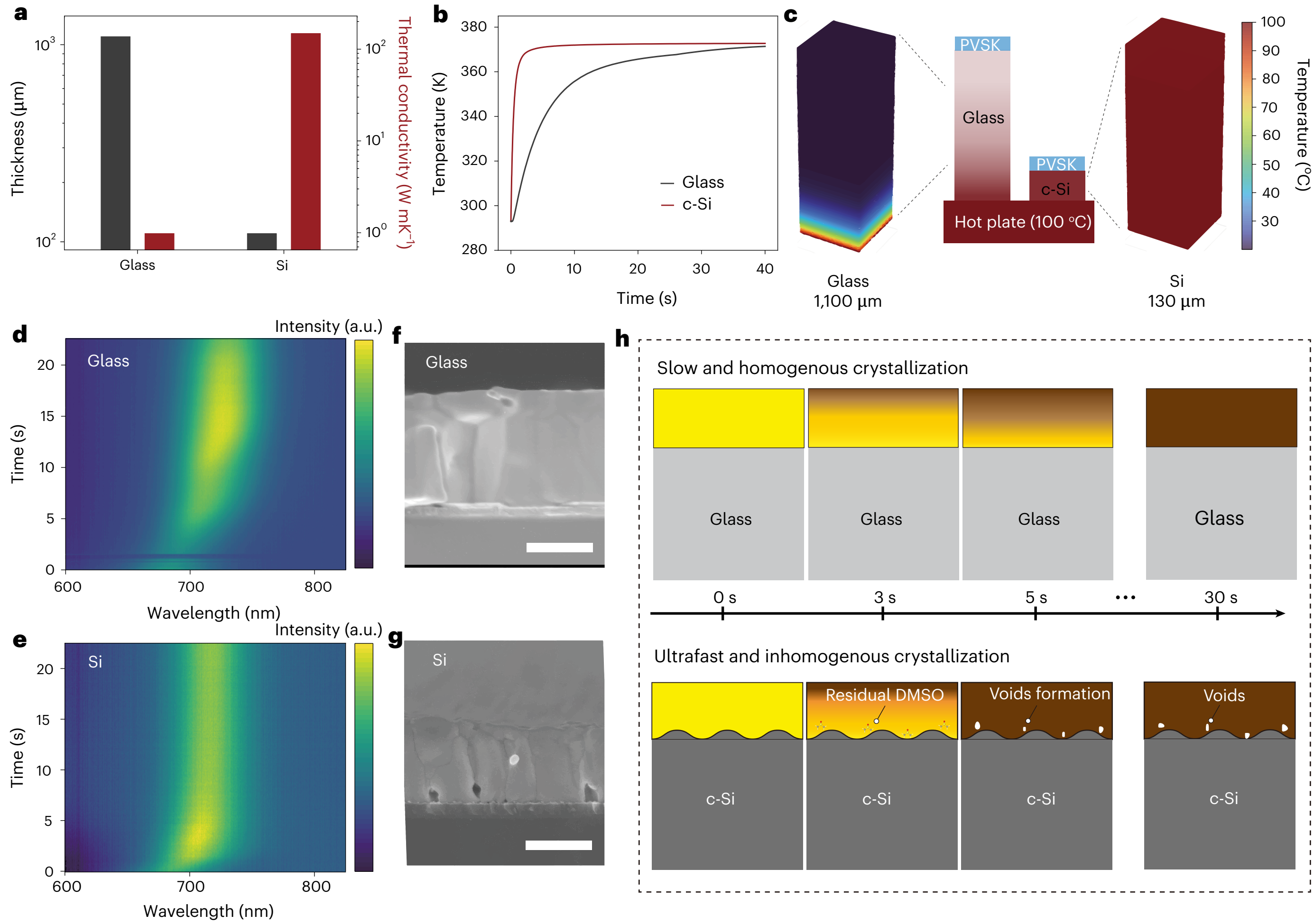

Fig. 1 | Thermal properties, crystallization dynamics and morphological comparison of perovskite films on glass and c-Si substrates. a, Visual summary of thickness and thermal conductivity properties of glass and c-Si substrates. **b**, Simulated annealing temperature profiles on glass and c-Si substrates. **c**, 3D temperature profile at the first second of heating on glass and c-Si substrates. The simulation domain dimensions are 180 × 180 × 1,100 μm^3 for the glass case and 180 × 180 × 130 μm^3 for the Si case. **d**,**e**, In situ photoluminescence (PL) spectra showing emissions peak evolution during crystallization on glass and c-Si. **f**,**g**, Cross-section SEM images of perovskite films on glass and c-Si. The scale bar is 0.5 μm. **h**, Schematic representation of crystallization mechanisms on glass and c-Si substrates.

cation—methylammonium (MA^+)[38], as evidenced in single-junction devices[23,28], perovskite crystallization on silicon substrates remains problematic, where the process is still excessively rapid. This limitation underscores the need to move beyond conventional more inorganic-cations-focused regulation strategies (hereafter referred to as ‘inorganic control’) and to explore the largely underdeveloped pathway of organic cation regulation (‘organic control’), in which FA^+ constitutes the dominant cation (~80 mol%). By directly targeting the principal FA^+ organic cations, we aim to tailor perovskite crystallization specifically for industrial Si-based tandem devices.

Therefore, we identify 2-Mercaptobenzothiazole (MBT) as a ligand capable of binding with organic cations (FA) to regulate the crystal growth of perovskite films. Here we adopt the broader chemical convention[39–41], using the term ‘ligand’ to describe MBT as an organic binding molecule targeting and interacting with FA^+, rather than in the narrower coordination chemistry sense. Notably, as shown in Fig. 2b, this ligand features dual-mode binding ability—specifically the heterocyclic N atom and the thiol (-SH) group—that enable simultaneous hydrogen bonding and electrostatic interaction with FA cations. This type of dual-mode interactions provides a stronger and more stable intermolecular interactions compared to single-site binding. This mechanism is similar to the commonly applied mechanism of chelation with PbI_2 in the inorganic control strategy, which provides multiple binding points with Pb that regulates the crystallization process[31,42–44].

Specifically, unlike previously reported multi-binding ligands that primarily interact with inorganic Pb^{2+}, MBT primarily works through dual-site interactions with FA^+—the principal organic cation in wide-bandgap perovskites. This substantially differentiates our ligand MBT from the majority of reported effective ligands for perovskite crystallization regulation strategy. Such a organic-cation-focused approach supplements conventional ‘inorganic control’ approach and is especially valuable for resolving the rapid crystallization challenges observed on thermally conductive Si substrates.

To demonstrate the dual-site and dual-mode binding ability of MBT with FA cations, we conduct electrostatic potential (ESP) mapping and nuclear magnetic resonance (NMR) spectroscopy. On the one hand, The N atom at the heterocyclic ring in MBT is most likely to form hydrogen bond with ammonium H atoms (N···H–N) in FA as it is the most electron-rich part of the ligand (Fig. 2a and Supplementary Fig. 5). From ^1H NMR results shown in Fig. 2c, the splitting of H atoms from $-NH_2$ group in FA at 8.73 ppm was observed, which resulted from the spin coupling between FA cations and ligands[45,46]. This confirms the formation of hydrogen bonds between FA cation and MBT. On the other hand, the H atom of the thiol group is the most electron-poor site of the MBT ligand (Fig. 2a), thus it is likely to interact with ammonium group in FA

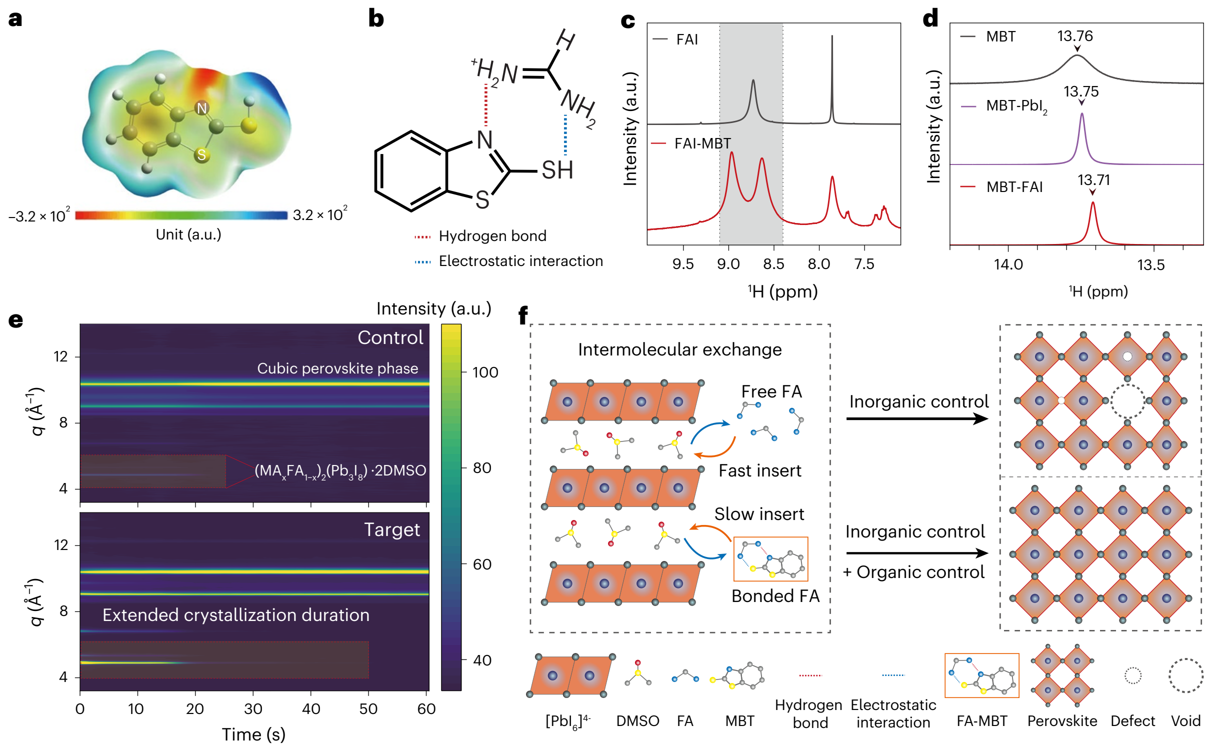

Fig. 2 | Mechanistic insights into organic control via ligand interaction with FA and its impact on crystallization dynamics. **a**, ESP mapping of the ligand molecule, showing regions of high electron density that facilitate hydrogen bonding. **b**, Schematic representation of the dual-mode hydrogen bonding and electrostatic interaction between MBT and FA cation. **c**, Nuclear magnetic resonance (NMR) spectra comparing FAI in the absence and presence of the ligand. The shaded background highlights the splitting of H atoms from $-NH_2$ group in FA. **d**, NMR spectra comparing ligand interactions with PbI_2 and FAI. The signal of the H atom from the thiol group in MBT is highlighted. **e**, In situ GIWAXS measurements for control and target samples during annealing. **f**, Schematic representation of the crystallization mechanisms. Panel **a** created with Gaussian 09[60].

cations through the intermolecular electrostatic force. The ^1H NMR in Fig. 2d and Supplementary Fig. 6 revealed an up-field chemical shift of the H atom from the thiol group, which confirms the electron-accepting behaviour of the thiol group from FA cations. It is noteworthy that the S atom from the thiol group in MBT can also form hydrogen bond (S… H–N) with FA because of its electronegativity. In addition, although the thiol group has the chemical potential to bind with PbI_2, the chemical shift of the H atom in the thiol group is negligible when MBT mixed with PbI_2. This indicates that MBT has a higher tendency to bind with FAI than with PbI_2, which is consistent with the density functional theory (DFT) calculations of the binding energy as shown in Supplementary Fig. 7. In conclusion, the MBT ligand shows the capability of dual-mode binding with FA cations through combined hydrogen bonding and electrostatic force, which can provide an effective control over FA cations.

Combining effective organic control with existing inorganic control can add an additional force, compared to sole control of inorganic Pb cations, to regulate and rationalize crystallization dynamics in perovskite deposition. Therefore, to demonstrate it, we introduce the ligand (1 mol%) into the precursor solution and investigated its impact on the crystallization dynamics of perovskites in the early stage during annealing through in situ grazing-incidence wide-angle X-ray scattering (GIWAXS) measurements (Fig. 2e). We refer to the perovskite films prepared using precursor with the ligand as target samples, and the films without ligand as control samples. All diffraction peaks indexed to the corresponding crystalline phases can be found in Supplementary Fig. 8a. We observed that the perovskite intermediate phases of $(MA_xFA_{1-x})_2(Pb_3I_8)\cdot 2DMSO$ (space group $Cmc2_1$) ($q = 4.9, 5.3, 6.8\ nm^{-1}$) forms before annealing[47], indicating that our strategy does not alter the perovskite intermediate phases. However, the target sample exhibits a prolonged retention of these intermediate phases during annealing, suggesting an extended crystallization process that facilitates a retarded and homogeneous crystallization pathway (Fig. 2e and Supplementary Fig. 8b). This prolonged retention is attributed to the more stable interaction between FAI and MBT, where the dual-mode binding effect—through hydrogen bonding and electrostatic force at both the heterocyclic N atom and H atom in -SH group—stabilizes the intermediate phases. This stabilization prevents premature transition to the perovskite phase, thereby enabling a more controlled and uniform crystallization process (Fig. 2f).

It is noteworthy that although MBT also has the potential to coordinate with DMSO (Supplementary Fig. 9), this interaction could only occur with free DMSO molecules that are not coordinating to PbX_2 (X = I, Br), as there is no new signal representing the expanded PbX_2-DMSO phase. Therefore, during the intermolecular exchange process between FAI and DMSO, MBT primarily interacts with FA cations. However, MBT could interact with free DMSO and retard its evaporation to further slow down the crystallization. In situ PL measurements (Supplementary Fig. 10) further corroborate the role of MBT in modulating perovskite crystallization on Si. Without MBT, the PL intensity rises sharply within the first few seconds, indicating rapid solvent loss and accelerated crystallization. By contrast, with MBT, the PL intensity exhibits an initial decrease followed by gradual recovery within ~5–20 s, closely resembling the behaviour observed on glass. This modified PL evolution demonstrates that MBT retards DMSO volatilization and FAI–DMSO exchange, thereby slowing crystallization and enabling a more controlled growth process on Si.

Optimized perovskite films with reduced non-radiative losses

As shown in Fig. 3a–d, the slower crystallization process in the target sample yields a more dense and uniform perovskite film morphology. SEM images of both the buried interface and cross section confirm this.

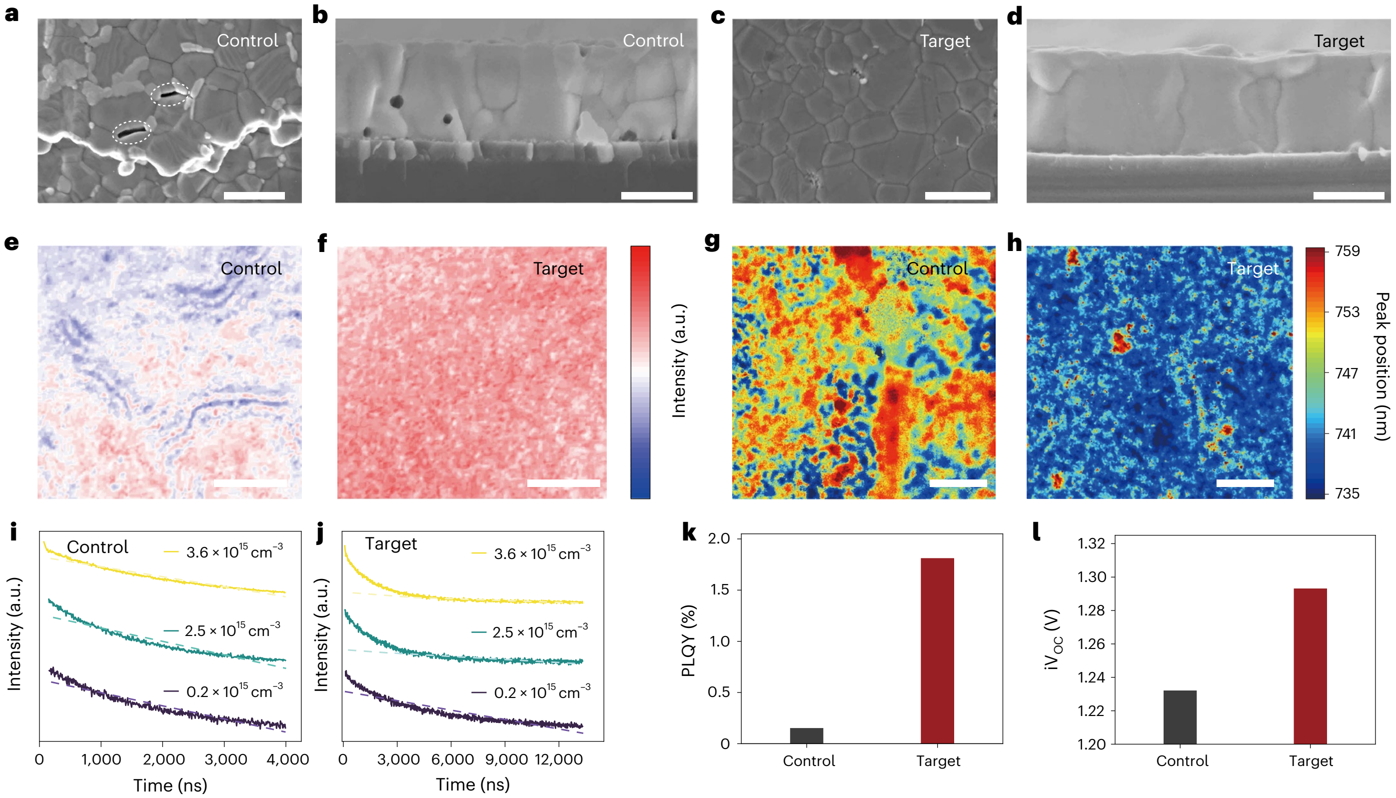

Fig. 3 | Morphological, optical and optoelectronic characterizations of perovskite films for control and target samples. a–**d**, SEM images of the top-view (left) of the buried interfaces and cross-sectional (right) morphology of control and target films. The scale bar for **a** and **c** is 1 µm, the scale bar for **b** and **d** is 0.5 µm. **e**,**f**, Steady-state confocal photoluminescence (PL) maps showing PL intensity and uniformity in the control and target perovskite films. The scale bar is 10 µm. **g**,**h**, Hyperspectral imaging maps illustrating the emission peak position information. The scale bar is 20 µm. **i**,**j**, Time-resolved photoluminescence (TRPL) decay curves at various carrier densities for control and target samples. The fitting routine can be found in the Supplementary Note 1. **k**,**l**, Optoelectronic performance comparison including photoluminescence quantum yield (PLQY) and iV_{OC}.

In contrast, the control sample without MBT shows prominent voids and non-uniformities in the bulk and buried interface regions, and pronounced surface wrinkling (Supplementary Fig. 11b), caused by rapid, uncontrolled crystallization that disrupts film integrity, which compromise optoelectronic properties. Whereas the MBT-treated film is free of voids and morphological discontinuities, highlighting enhanced crystallinity and homogeneity. The Atomic Force Microscopy (AFM) height maps further confirm a smoother surface for the MBT-treated film, whereas the control shows pronounced roughness (Supplementary Fig. 12a,b and Supplementary Table 1). These results demonstrate that MBT stabilizes intermediate phases, enabling controlled crystallization with improved crystal quality, which collectively lead to high-quality perovskite films on industrial silicon wafers. It is noted that the beneficial role of MBT in regulating crystallization and inhibiting void formation is preserved when moving from planar Si to textured Si substrates (Supplementary Fig. 13).

To assess the enhancement of optoelectronic properties for perovskite films grown on thin c-Si, confocal photoluminescence (PL) imaging is performed (Fig. 3e,f). The results reveal that compared to the control sample, the target film exhibited pronounced stronger and more uniform PL emissions across the entire detection area, indicative of a decrease in defect density and improvement in film morphology. The perovskite film heterogeneity has been a continuous challenge to achieve high-quality light absorber, thus the uniformity of element distribution (Supplementary Fig. 14) and the λ_{em} peak maximum map (Fig. 3g, h) through the X-ray fluorescence measurement the hyperspectral imaging microscope, respectively, were conducted to assess phase homogeneity. While the target perovskite film displays most occurring PL peaks at 735 nm (1.69 eV) on CZ Si wafer, the control perovskite film displays the most occurring PL peaks at 750 nm (1.65 eV) on CZ Si wafer, the lower PL peak can be attributed to compositional inhomogeneity and partial degradation during measurement. The histograms of the hyperspectral images are provided in the Supplementary Fig. 15. The Kelvin Probe Force Microscopy (KPFM) potential maps also confirm more homogeneous potential distribution for the target sample, compared to the control sample, suggesting improved surface electronic uniformity (Supplementary Fig. 16). The suppression of the red shift and the improved uniformity of element and potential distribution for the target sample confirms that the rationalized perovskite crystallization process facilitated formation of homogeneous perovskite films on CZ Si wafers. Time-of-Flight Secondary Ion Mass Spectrometry (TOF-SIMS) profile of perovskite films with MBT deposited on thin Si indicates that MBT is primarily located at the top and bottom interfaces of the perovskite layer (Supplementary Fig. 17). There may be trace incorporation at grain boundaries or in the bulk, but the concentration is too low to be reliably detected. Given MBT's ability to form hydrogen bonds and electrostatic interactions, it may contribute to a certain extent to interfacial defect passivation.

We carry out time-resolved photoluminescence (TRPL) for perovskite films to quantify the charge carrier lifetime in the control and target samples (Fig. 3i,j and Supplementary Fig. 18). We extract the average radiative lifetime through a mono-exponential decay equation, the lifetime for the target sample is three times longer than the control sample, indicating a decrease in the non-radiative recombination loss in the target film. To further quantify trap-assistant recombination rates, we further investigated non-radiative recombination processes

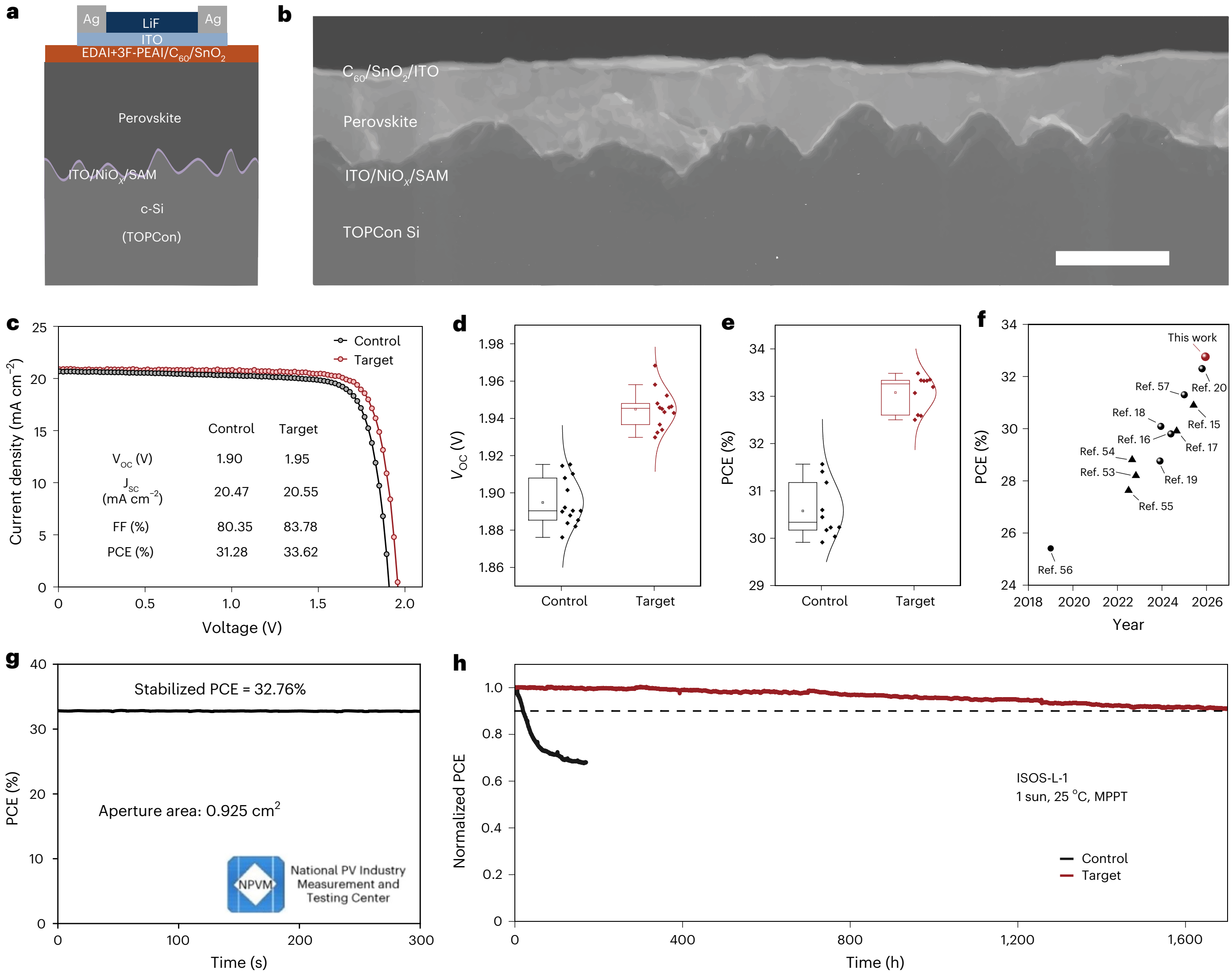

Fig. 4 | Device architecture, performance and stability evaluation of perovskite/silicon tandem solar cells. a, Schematic illustration of the tandem device architecture. **b**, Cross-sectional SEM image of the tandem device. The scale bar is 2 μm. **c**, Current density–voltage (*J*–*V*) characteristics of control and target tandem devices. **d**,**e**, Statistical distributions of V_{OC} and PCE for control and target devices (14 devices for each type). Box plots are defined as follows: the centre line represents the median; the box bounds represent the first and third quartiles (25th and 75th percentiles); the whiskers extend to the minima and maxima (the lowest and highest data points). **f**, Summary of the PCEs for the state-of-the-art TOPCon tandems, with spheres and triangles respectively representing certified and non-certified PCEs[15–20,53–57]. **g**, Certified stabilized efficiency of the target tandem device by NPVM. **h**, Long-term operational stability of control and target tandem devices under continuous illumination (ISOS-L-1 protocol, 1 sun, 25 °C, maximum power point tracking). The starting efficiencies for the encapsulated target and control tandem devices are 29.15% and 26.47%, respectively. Credit: **g**, NPVM.

in perovskite films grown on c-Si substrates. Thus, fluence-dependent TRPL measurements are conducted with the injection carrier density from 2.0×10^{14} cm^{-3} to 3.6×10^{16} cm^{-3}. The extracted trap-assistant recombination rates are 3.2×10^5 and 4.3×10^4 cm s^{-1} for the control and target sample, respectively, revealing a substantially reduced non-radiative recombination rate in the optimized perovskite films. To the best of our knowledge, the optimized sample exhibits one of the lowest trap-assisted recombination rates reported to date, which confirms a minimized non-radiative recombination in the perovskite layer through our strategy[48–51]. Additionally, photoluminescence quantum yield (PLQY) measurements demonstrate a quantum yield of 1.80% for the target perovskites in a full device stack (Si/ITO/NiO$_X$/self-assembled monolayer (SAM)/Perovskite/surface treatment/C$_{60}$/SnO$_2$/ITO), much higher than the PLQY of 0.15% for the control perovskites (Fig. 3k,l). Moreover, this high PLQY corresponds to an iV$_{OC}$ exceeding 1.29 V, representing an enhancement of 60 mV compared to the control sample. This is among the highest reported iV$_{OC}$ or quasi-Fermi level splitting values for a full device stack under 1-sun equivalent illumination for wide-bandgap perovskites (~1.70 eV) designed for c-Si-based tandem solar cells[52].

Rationalized perovskites for TOPCon tandem solar cells

To evaluate the performance of perovskite films in tandem solar cells, devices with a 0.925 cm^2 active area were fabricated, using industrial TOPCon c-Si bottom cells as shown in Fig. 4a. The cross-sectional SEM image of the tandem solar cell shows the complete coverage of perovskite top cell on c-Si bottom cell featuring a textured surface with widely distributed pyramid sizes (Fig. 4b and Supplementary Fig. 19).

The photovoltaic performance of perovskite/TOPCon tandem solar cells was then investigated. Figure 4c demonstrates the current density–voltage (*J*–*V*) curves of the best-performing target and control tandem solar cells, respectively. The target tandem device exhibits a higher fill factor (FF) of 83.78% than that of the control device with a FF of 80.35%. The FF gain is mainly attributed to reduced trap-assisted recombination and improved carrier lifetime. Notably, the target device achieves an impressive V_{OC} of 1.95 V; this corresponds to a V_{OC} enhancement of ~50 mV compared to control device with a V_{OC} of 1.90 V, demonstrating one of the highest reported V_{OC}s for perovskite/TOPCon tandem solar cells. This advancement enabled a power conversion efficiency of 33.62% for perovskite/TOPCon tandem solar cells, outperforming its control counterpart with a PCE of 31.28%, we attribute this improvement to the rationalized crystal growth, optimized film morphology and minimized non-radiative recombination of the perovskite layer after the addition of organic control. The statistics of the photovoltaic performance for control and target tandem devices can be found in Supplementary Fig. 20. Figure 4d,e shows the statistics of the V_{OC} and PCE values of the control and target perovskite/TOPCon tandems, highlighting the effective enhancement of V_{OC} and PCE with good reproducibility of our strategy. The external quantum efficiency (EQE) spectra of both sub-cells (Supplementary Fig. 21) yield integrated current densities of 20.31 and 20.30 mA cm^{-2} for the top and bottom cells, respectively, in good agreement with the measured J_{SC}. We also carry out electroluminescence imaging (EL) for the control and target tandem devices (Supplementary Fig. 22), and the target device shows substantially more uniform EL intensity, reflecting improved charge transport and enhanced film quality. We sent our perovskite/TOPCon tandem solar cell to NPVM for third-party independent measurement (Supplementary Fig. 23), and we achieved a certified power conversion efficiency of 32.54% with negligible hysteresis (Supplementary Fig. 23) and a 300 s maximum power point tracking (MPPT) efficiency of 32.76% (Fig. 4g). This is among the highest reported certified stabilized efficiencies for monolithic perovskite/TOPCon tandem solar cells. Figure 4f summarizes the previous state-of-the-art PCEs reported for two-terminal monolithic perovskite/TOPCon tandem solar cells[15–20,53–57]. Detailed information of device performance of these tandem solar cells can be found in Supplementary Table 2.

To evaluate the stability of our perovskite/TOPCon tandems solar cells, the tandem devices were encapsulated to measure their operational stability in ambient air according to ISOS-L-1 protocol[58]; the starting PCEs of the encapsulated target and control tandem devices before stability testing were 29.15% and 26.47%, respectively. As shown in Fig. 4h, the target tandem device retained 91% of its initial PCE for nearly 1,700 h continuous operation under MPPT conditions at room temperature and relative humidity of 85%; it outperforms the control device, which degrades more rapidly, indicating considerably improved device stability. These results underscore the substantial stability enhancement achieved through rationalized crystallization and defect suppression strategies, further validating the suitability of this approach for industrial applications.

Conclusions

We identify key challenges in perovskite film quality on industrial c-Si bottom cells, where the high thermal conductivity and low thermal mass of Si wafers accelerate heat transfer, causing rapid crystallization and defects. To address this, we introduce a dual-mode binding ligand with formamidinium cations, which regulates crystallization dynamics and improves film quality on industrial TOPCon Si wafers. This approach enhances morphology and optoelectronic properties, enabling high-quality perovskite integration. As a result, our tandem devices achieve a certified PCE of 32.76%, advancing high-performance tandem photovoltaics for future mainstream TOPCon technology. In addition, we believe our strategy holds potential to be applied in industrial production lines using scalable and high-throughput solution processing methods[58] to bridge our research to industrial application.

Methods

Materials

Caesium iodide (CsI), lead iodide (PbI_2), lead bromide ($PbBr_2$) and 2-Mercaptobenzothiazole (MBT) were purchased from TCI Chemicals. Formamidinium iodide (FAI) and methylammonium bromide (MABr) were purchased from Greatcell Solar Materials. *N*, *N*-dimethylformamide (DMF, anhydrous, 99.8%), dimethyl sulfoxide (DMSO, anhydrous, 99.9%), isopropanol (anhydrous, 99.5%) and chlorobenzene (CB, anhydrous, 99.8%) were purchased from Sigma Aldrich. Ph-4PACz was synthesized according to our previous report[51]. Unless stated otherwise, all materials were used as received.

Silicon solar cells fabrication

In this study, an industrially viable TOPCon cell fabrication process was employed. The silicon wafers utilized were Czochralski-grown, phosphorus-doped n-type monocrystalline silicon, with a resistivity ranging from 0.3 to 1.2 Ω·cm and dimensions of approximately 182.3 mm × 183.75 mm. The wafers, with a thickness of around 130 µm, underwent industrial alkaline texturing using a KOH and organic additive solution. A boron emitter was then created in a boron diffusion furnace using a BCl_3 source. Subsequent steps included a single-sided HF treatment and an alkaline texturing process to eliminate the rear diffused layers. A thin thermal oxide layer was grown on the rear side, followed by the deposition of intrinsic poly-Si via low-pressure chemical vapour deposition. The intrinsic poly-Si was doped in a $POCl_3$ diffusion furnace to form n+ poly-Si. A single-sided HF process and a KOH etch were applied to remove the front-side wrap-around poly-Si. The front-side borosilicate glass and rear phosphosilicate glass layers were etched away using HF and cleaned with RCA clean (standard wafer cleaning procedure) and deionized (DI) water solutions. The textured surface was passivated using atomic layer deposition (ALD) of Al_2O_3 and capped with plasma-enhanced chemical vapor deposition (PECVD) SiN_x. The 20-nm ITO layer was deposited as a interconnection layer using a high-temperature process at 450 °C. Due to the relatively thick n-type poly-Si layer beneath, the TOPCon bottom cell is sufficiently robust against sputter-induced damage, and no additional protective measures were necessary during ITO deposition.

Tandem solar cells fabrication

A 1.8 M $Cs_{0.05}MA_{0.15}FA_{0.8}Pb(I_{0.755}Br_{0.255})_3$ perovskite precursor was prepared by dissolving CsI, MABr, FAI, $PbBr_2$ and PbI_2 in a mixture of DMF and DMSO (4:1 v/v). A deep-yellow-coloured precursor was formed by stirring at 60 °C for 2 h and then filtered using a 0.45 µm polytetrafluoroethylene (PTFE) membrane before use. A 1 mol% ligand of MBT was added to the solution for the target precursor; the concentration was determined through an optimization study (Supplementary Fig. 24). The TOPCon Silicon bottom cells with ITO were first treated by ultraviolet ozone for 10 min and then immediately transferred to a sputtering tool to deposit 15 nm NiO_x film. Then, the silicon bottom cells were transferred to a N_2-filled glovebox. The Ph-4PACz (1 mg ml^{-1} in IPA) was spin coated on the Si at 4,000 rpm for 30 s, followed by annealing at 100 °C for 10 min. Then, the perovskite precursor was spin coated at 1,000 rpm for 15 s (acceleration rate 500 rpm s^{-1}), 3,500 rpm for 35 s (acceleration rate 1,000 rpm s^{-1}) and 7,000 rpm for 12 s (acceleration rate 2,000 rpm s^{-1}), respectively. At the start of the third step, 200 µl CB was dropped as antisolvent. The films were then annealed at 100 °C for 30 min. Then, a mixed solution of 1 mg $EDAI_2$ and 1 mg 3F-PEAI in 1 ml IPA was spin coated at 4,000 rpm for 30 s, followed by annealing at 100 °C for 5 min for perovskite surface passivation, according to our previous report[26]. Then, 12 nm C_{60} was deposited by a thermal evaporator, 10 nm SnO_2 was deposited by ALD system, then the cells were transferred to a magnetron sputtering system to deposit 40 nm ITO. Then, 500 nm silver frame and fingers were deposited by a thermal evaporator. Finally, 100 nm LiF was deposited by a thermal evaporator to finish the tandem device. The back contact of the tandem was realized by thermal evaporation of a 500 nm silver.

Device testing

The in-house current density–voltage (*J*–*V*) measurements of the perovskite/TOPCon tandem solar cells were recorded with SINUS-220, Wavelabs under simulated 1-sun AM 1.5 G illumination (100 mW cm^{-2}) in air, with a scanning rate of 100 mV s^{-1} (voltage step of 10 mV and delay time of 200 ms). The active area was determined by the aperture shade mask with an area of 0.925 cm^2 placed on top of the tandem solar cells. The Class AAA solar simulator's irradiance was calibrated using secondary World PV Scale (WPVS) reference device (traceable to primary WPVS reference device calibrated at Institute for Solar Energy Research Hamelin (ISFH)), using IEC60904-1(2020) method. No spectral mismatch factor correction was applied.

Stability testing

For the stability tests, the tandem devices were encapsulated between two glasses with butyl rubber edge sealant and polyolefin elastomer (POE) encapsulant, which were laminated in a laminator (EVG 501) at 100 °C for 10 min. Metal strips were used to extend the electrodes of the devices to the outside of the glass. The MPPT of the encapsulated tandem devices were measured with MPP Tracking-4B source measure unit system (Shenzhen Lancheng Technology Co. Ltd.) under a 100 mW cm^{-2} light-emitting diode (LED). The measurements were carried out in ambient atmosphere at a temperature of 25 °C and about 85% relative humidity.

SEM characterization

SEM images were taken with Regulus SU8200 system (Hitachi) at 3 kV accelerating voltage under SE mode. The SEM samples on ITO glass (Fig. 1f,g) and TOPCon Si substrates (Fig. 3a–d and Supplementary Figs. 4, 11 and 13) were prepared using the the same stack configuration (Substrate/ITO/NiO$_X$/SAM/Perovskite) to ensure consistency and avoid the underlying layer influencing the crystallization behaviour and film morphology. The cleaning and deposition procedures strictly follow those used for device fabrication; the SEM samples for buried interfaces were prepared as follows. Two as-prepared half-cells (Si/ITO/NiO$_X$/SAM/Perovskite) were immediately transferred into wafer bonding tool (EVG 501). In a vacuum environment, the two half-cells were piled perovskite to perovskite and annealed under ~1.6 MPa at 100 °C for 10 min. Afterward, the bonded samples were taken out and separated by applying tensile force. One can observe on a half-cell that the dark area represents the buried perovskite on local interface.

Other characterizations

Grazing-incidence X-ray scattering (GIWAXS) studies were performed at the BL14B1 beamline of the Shanghai Synchrotron Radiation Facility. A beam of 23 × 32 µm^2 shape with a monochromatic X-ray wavelength of 1.24 Å and a high brilliance impinged the samples at an incidence angle of 1° to probe the sample. For GIWAXS, a Mar 225 detector was used with a sample-to-detector distance of 365 mm. Data reduction was performed with DPDAK software[59]. Si attenuation of 2.33 mm^{-1} and horizontal polarization of 0.98 was used, and an air attenuation coefficient of 3.01×10^{-4} mm^{-1} was used for GIWAXS. The beam centre was measured directly by applying the X-ray absorbers, and the LaB6 sample was calibrated for the sample-to-detector distance. In situ photoluminescence (PL) spectra were recorded using a USB 2000+ spectrometer (Ocean Optics) equipped with a 1,000-µm optical fibre inside an N$_2$ glovebox. The excitation was provided by a UV lamp emitting light at a wavelength of 365 nm. The nuclear magnetic resonance (NMR) spectra were recorded on a Bruker Ascend 400 MHz spectrometer using DMSO-d6 as the solvent and tetramethylsilane as the reference. The NMR samples were prepared by dissolving the different combinations of materials (MBT, FAI or PbI$_2$) in DMSO-d6. Electrostatic surface potential (ESP) simulations and the graphic of chemical structure in Fig. 2a were calculated and created by Gaussian 09 program package with B3LYP/6-311 G basis[60]. Confocal PL mapping was measured on a Nikon A1 confocal microscope equipped with a 633 nm continuous-wave laser. For hyperspectral microscope characterization, wide-field hyperspectral microscopy measurements were conducted using the Photon etc. IMA model. We employed ×20 air objective lenses from Olympus (MPLFN), which were specifically chromatic aberration corrected. We utilized a continuous-wave laser with a wavelength of 405 nm. A dichroic mirror was utilized to filter the excitation laser. The emitted light from the sample was directed onto a volume Bragg grating, which spectrally separated the light and directed it onto a CCD camera. The CCD camera, maintained at 0 °C with a thermoelectric cooler, had a resolution of 1,024 × 1,024 pixels and operated within a wavelength range of 650–850 nm. By varying the angle of the grating concerning the incident light, we obtained the spectral information for the light emanating from each point on the sample. Fluence-dependent TRPL measurements were conducted by PicoQuant FluoTime 300 spectrometer. After tuning the lens to its optimum position, the steady-state PL and the lifetime measurement are conducted with laser excitation at 515.8 nm in ambient air with the films encapsulated. The power densities were recorded by Thorlabs PM16-130, and the beam size was measured by beam profiler (BC207VIS(/M)). Photoluminescence quantum yield (PLQY) measurements were performed using the LuQY Pro system from Quantum Yield Berlin, with a 515 nm laser providing equivalent 1-sun intensity laser. EQE was conducted with the Quantum Efficiency Measurement System with voltage bias and multiple LED source bias (Enlitech). AFM and KPFM measurements were conducted with the Park NX20 system. AFM measurements were conducted with non-contact mode. Frequency modulation mode (sideband KPFM) was applied throughout the measurements to obtain better contrasts and higher resolution. Time-of-Flight Secondary Ion Mass Spectrometry (TOF-SIMS) analysis was performed using an IONTOF TOF-SIMS.5 instrument under 3.1×10^{-8} mbar vacuum. A pulsed Bi^{1+} primary beam set at 30 keV was utilized for analysis, operating in random raster mode with a scanning area of 100 × 100 µm^2.

Heat transfer simulation model

To analyse the heating process, a finite volume model is adopted for the thermal conduction simulation[61].

$$\rho \frac{\partial h}{\partial t} = \nabla \cdot (k \nabla T)$$

where ρ and k are the density and thermal conductivity of the material. h and T are the specific enthalpy and temperature. On the surface, the heat convection and radiation conditions are adopted. The bottom is a fixed temperature condition to heat the glass and silicon and then heat the perovskite. The material properties of the glass and silicon are listed in Supplementary Table 3 [32].

DFT calculations

All the spin-polarized density functional theory (DFT) calculations were performed with the Vienna Ab initio Simulation Package (5.4.4 version) under the framework of projector augmented wave method[62,63]. The generalized gradient approximation of the Perdew–Burke–Ernzerhof functional was employed as the exchange-correlation functional[64]. The valence wave functions were expanded by plane wave with a cut-off energy of 400 eV, while all the structures were optimized until the force on each atom was less than 0.02 eV Å^{-1}. The neural molecules MBT was optimized in a 25 Å x 25 Å x 25 Å unit cell. Then a pair of PbI$_2$ or FAI was added into the model to calculate the interaction strength between

MBT and PbI_2/FAI. The binding energy was calculated according to the following equation:

$$E_{\mathrm{binding}} = E_{\mathrm{MBT+PbI_2/FAI}} - E_{\mathrm{MBT}} - E_{\mathrm{PbI_2/FAI}}$$

Reporting summary

Further information on research design is available in the Nature Portfolio Reporting Summary linked to this article.

Data availability

The data that support the findings of this study are available within the Article and its Supplementary Information.

References

1. *Photovoltaics Report* (Fraunhofer ISE, 2024).
2. Chunduri, S. Next-gen solar cell technologies & projections. *TaiyangNews - All About Solar Power* https://taiyangnews.info/technology/next-gen-solar-cell-technologies-projections (2025).
3. Feldmann, F., Bivour, M., Reichel, C., Hermle, M. & Glunz, S. W. Passivated rear contacts for high-efficiency n-type Si solar cells providing high interface passivation quality and excellent transport characteristics. *Sol. Energy Mater. Sol. Cells* **120**, 270–274 (2014).
4. Yan, D. et al. Polysilicon passivated junctions: the next technology for silicon solar cells?. *Joule* **5**, 811–828 (2021).
5. Deng, S. et al. Mitigating parasitic absorption in Poly-Si contacts for TOPCon solar cells: a comprehensive review. *Sol. Energy Mater. Sol. Cells* **267**, 112704 (2024).
6. Aydin, E. et al. Pathways toward commercial perovskite/silicon tandem photovoltaics. *Science* **383**, eadh3849 (2024).
7. Duan, L. et al. Stability challenges for the commercialization of perovskite–silicon tandem solar cells. *Nat. Rev. Mater.* **8**, 261–281 (2023).
8. Fu, F. et al. Monolithic perovskite-silicon tandem solar cells: from the lab to fab?. *Adv. Mater.* **34**, 2106540 (2022).
9. Trinasolar Unveils i-TOPCon Ultra Technology, with Cell Efficiency of 26.58%. *Trina Solar* https://static.trinasolar.com/en-apac/resources/newsroom/aptrinasolar-unveils-i-topcon-ultra-technology-cell-efficiency-2658 (2024).
10. Wagner, P. et al. Bandgap pairing in three-terminal tandem solar cells: from limiting efficiency to voltage-matched device performance. *Sol. RRL* **8**, 2300963 (2024).
11. Liu, J. et al. Perovskite/silicon tandem solar cells with bilayer interface passivation. *Nature* **635**, 596–603 (2024).
12. Ugur, E. et al. Enhanced cation interaction in perovskites for efficient tandem solar cells with silicon. *Science* **385**, 533–538 (2024).
13. Wu, W. et al. Stable and uniform self-assembled organic diradical molecules for perovskite photovoltaics. *Science* **389**, 195–199 (2025).
14. Jia, L. et al. Efficient perovskite/silicon tandem with asymmetric self-assembly molecule. *Nature* **644**, 912–919 (2025).
15. Luo, Y. et al. Inductive effects in molecular contacts enable wide-bandgap perovskite cells for efficient perovskite/TOPCon tandems. *Nat. Commun.* **16**, 4516 (2025).
16. Duan, L. et al. Over 29%-efficient, stable n–i–p monolithic perovskite/silicon tandem solar cells based on double-sided poly-Si/SiO_2 passivating contact silicon cells. *J. Mater. Chem. A* **12**, 20006–20016 (2024).
17. Li, B. et al. Atomic-layer-deposition-free monolithic perovskite/silicon tandem solar cell reaching 29.91% power conversion on industrial PERX/TOPCon-like silicon bottom cells. *ACS Energy Lett* **9**, 4550–4556 (2024).
18. Qiao, L. et al. Freezing halide segregation under intense light for photostable perovskite/silicon tandem solar cells. *Adv. Energy Mater.* **14**, 2302983 (2024).
19. Zheng, J. et al. Polycrystalline silicon tunnelling recombination layers for high-efficiency perovskite/tunnel oxide passivating contact tandem solar cells. *Nat. Energy* **8**, 1250–1261 (2023).
20. Wang, L. et al. Ultra-uniform perovskite film with minimized interconnection energy loss for efficient perovskite/TOPCon tandem solar cells. *Joule* **9**, 102174 (2025).
21. Elsmani, M. I. et al. Recent issues and configuration factors in perovskite-silicon tandem solar cells towards large scaling production. *Nanomaterials* **11**, 3186 (2021).
22. Ballif, C., Haug, F.-J., Boccard, M., Verlinden, P. J. & Hahn, G. Status and perspectives of crystalline silicon photovoltaics in research and industry. *Nat. Rev. Mater.* **7**, 597–616 (2022).
23. Chen, H. et al. Improved charge extraction in inverted perovskite solar cells with dual-site-binding ligands. *Science* **384**, 189–193 (2024).
24. Wang, J. et al. Halide homogenization for low energy loss in 2-eV-bandgap perovskites and increased efficiency in all-perovskite triple-junction solar cells. *Nat. Energy* **9**, 70–80 (2024).
25. Gao, H. et al. Homogeneous crystallization and buried interface passivation for perovskite tandem solar modules. *Science* **383**, 855–859 (2024).
26. Jiang, X. et al. Surface heterojunction based on n-type low-dimensional perovskite film for highly efficient perovskite tandem solar cells. *Natl Sci. Rev.* **11**, nwae055 (2024).
27. Zhang, T. et al. MA cation-induced diffusional growth of low-bandgap FA-Cs perovskites driven by natural gradient annealing. *Research* **2021**, 2021/9765106 (2021).
28. Yang, W. S. et al. High-performance photovoltaic perovskite layers fabricated through intramolecular exchange. *Science* **348**, 1234–1237 (2015).
29. Zhang, Y. et al. Synchronized crystallization in tin-lead perovskite solar cells. *Nat. Commun.* **15**, 6887 (2024).
30. Zuo, W. et al. Coordination chemistry as a universal strategy for a controlled perovskite crystallization. *Adv. Mater.* **35**, 2302889 (2023).
31. Chen, R. et al. Reduction of bulk and surface defects in inverted methylammonium-and bromide-free formamidinium perovskite solar cells. *Nat. Energy* **8**, 839–849 (2023).
32. Amalu, E. H. & Fabunmi, O. A. Thermal control of crystalline silicon photovoltaic (c-Si PV) module using Docosane phase change material (PCM) for improved performance. *Sol. Energy* **234**, 203–221 (2022).
33. Li, N. et al. Liquid medium annealing for fabricating durable perovskite solar cells with improved reproducibility. *Science* **373**, 561–567 (2021).
34. Huang, T. et al. Performance-limiting formation dynamics in mixed-halide perovskites. *Sci. Adv.* **7**, eabj1799 (2021).
35. Chen, S. et al. Stabilizing perovskite-substrate interfaces for high-performance perovskite modules. *Science* **373**, 902–907 (2021).
36. Zheng, X. et al. Co-deposition of hole-selective contact and absorber for improving the processability of perovskite solar cells. *Nat. Energy* **8**, 462–472 (2023).
37. Chen, S. et al. Crystallization in one-step solution deposition of perovskite films: upward or downward?. *Sci. Adv.* **7**, eabb2412 (2021).
38. Jeon, N. J. et al. Solvent engineering for high-performance inorganic–organic hybrid perovskite solar cells. *Nat. Mater.* **13**, 897–903 (2014).
39. McPhie, K. A. et al. Discovery and optimisation of a covalent ligand for TRIM25 and its application to targeted protein ubiquitination. *Chem. Sci.* **16**, 10432–10443 (2025).
40. Warner, K. D., Hajdin, C. E. & Weeks, K. M. Principles for targeting RNA with drug-like small molecules. *Nat. Rev. Drug Discovery* **17**, 547–558 (2018).
41. Assaf, K. I. & Nau, W. M. Cucurbiturils: from synthesis to high-affinity binding and catalysis. *Chem. Soc. Rev.* **44**, 394–418 (2015).

42. Fei, C. et al. Lead-chelating hole-transport layers for efficient and stable perovskite minimodules. *Science* **380**, 823–829 (2023).
43. Zou, Y. et al. Manipulating crystallization dynamics through chelating molecules for bright perovskite emitters. *Nat. Commun.* **12**, 4831 (2021).
44. Jiang, X. et al. One-step synthesis of $SnI_2{\cdot}(DMSO)_x$ adducts for high-performance tin perovskite solar cells. *J. Am. Chem. Soc.* **143**, 10970–10976 (2021).
45. Su, L. et al. Passivating defects via retarding the reaction rate of FAI and PbI_2 enables stable perovskite solar cells. *ACS Appl. Mater. Interfaces* **16**, 20755–20766 (2024).
46. Lu, Y. et al. Stabilization of organic cations in lead halide perovskite solar cells using phosphine oxides derivatives. *J. Am. Chem. Soc.* **146**, 22387–22395 (2024).
47. Guo, R. et al. Trace water in lead iodide affecting perovskite crystal nucleation limits the performance of perovskite solar cells. *Adv. Mater.* **36**, 2310237 (2024).
48. Nagane, S. et al. Tetrafluoroborate-induced reduction in defect density in hybrid perovskites through halide management. *Adv. Mater.* **33**, 2102462 (2021).
49. Richter, J. M. et al. Enhancing photoluminescence yields in lead halide perovskites by photon recycling and light out-coupling. *Nat. Commun.* **7**, 13941 (2016).
50. Bi, E. et al. Diffusion engineering of ions and charge carriers for stable efficient perovskite solar cells. *Nat. Commun.* **8**, 15330 (2017).
51. Wang, X. et al. Regulating phase homogeneity by self-assembled molecules for enhanced efficiency and stability of inverted perovskite solar cells. *Nat. Photonics* **18**, 1269–1275 (2024).
52. Mariotti, S. et al. Interface engineering for high-performance, triple-halide perovskite–silicon tandem solar cells. *Science* **381**, 63–69 (2023).
53. Ying, Z. et al. Monolithic perovskite/black-silicon tandems based on tunnel oxide passivated contacts. *Joule* **6**, 2644–2661 (2022).
54. Sveinbjörnsson, K. et al. Monolithic perovskite/silicon tandem solar cell with 28.7% efficiency using industrial silicon bottom cells. *ACS Energy Lett* **7**, 2654–2656 (2022).
55. Wu, Y. et al. 27.6% perovskite/c-Si tandem solar cells using industrial fabricated TOPCon device. *Adv. Energy Mater.* **12**, 2200821 (2022).
56. Nogay, G. et al. 25.1%-efficient monolithic perovskite/silicon tandem solar cell based on ap-type monocrystalline textured silicon wafer and high-temperature passivating contacts. *ACS Energy Lett* **4**, 844–845 (2019).
57. Wang, L. et al. Highly efficient monolithic perovskite/TOPCon silicon tandem solar cells enabled by 'halide locking'. *Adv. Mater.* **37**, 2416150 (2025).
58. Khenkin, M. V. et al. Consensus statement for stability assessment and reporting for perovskite photovoltaics based on ISOS procedures. *Nat. Energy* **5**, 35–49 (2020).
59. Benecke, G. et al. A customizable software for fast reduction and analysis of large X-ray scattering data sets: applications of the new DPDAK package to small-angle X-ray scattering and grazing-incidence small-angle X-ray scattering. *J. Appl. Crystallogr.* **47**, 1797–1803 (2014).
60. Frisch, M. J. et al. Gaussian 09, Revision C.01 (Gaussian, Inc., 2016).
61. Eymard, R. Finite volume methods. *Handb. Numer. Anal.* **7**, 713 (2000).
62. Kresse, G. & Furthmüller, J. Efficient iterative schemes for ab initio total-energy calculations using a plane-wave basis set. *Phys. Rev. B* **54**, 11169 (1996).
63. Kresse, G. & Joubert, D. From ultrasoft pseudopotentials to the projector augmented-wave method. *Phys. Rev. B* **59**, 1758 (1999).
64. Perdew, J. P., Burke, K. & Ernzerhof, M. Generalized gradient approximation made simple. *Phys. Rev. Lett.* **77**, 3865 (1996).

Acknowledgements

Y.H. acknowledges the support from Agency for Science, Technology and Research (A*STAR) under its Materials Technology Cluster Industrial Research Grant (M23M6c0108). Q.Z., R.G., S.L., N.L., Z.S., X.G., H.L., Z.D., J.C., Y.-D.W., R.L., X.W., Z.J., L.K.L., D.L. and Y.H. are affiliated with the Solar Energy Research Institute of Singapore (SERIS), a research institute at the National University of Singapore (NUS). SERIS is supported by the National University of Singapore (NUS), the National Research Foundation Singapore (NRF), the Energy Market Authority of Singapore (EMA) and the Singapore Economic Development Board (EDB). This work was supported in part by the BL14B1 beamline of Shanghai Synchrotron Radiation Facility (SSRF), Shanghai, China. We would like to acknowledge that computational work involved in this research work is partially supported by NUS IT's Research Computing group under grant number NUSREC-HPC-00001.

Author contributions

Q.Z. and Y.H. conceived the idea and designed the experiments. Y.H. directed and supervised the project. M.X., J.W., X.Z., J.Y. and H.J. fabricated the Si bottom cells. Q.Z., M.X., J.W., X.Z., J.Y. and H.J. fabricated the perovskite tandem solar cells. Q.Z. conducted film fabrication and characterizations. X.J., C.-H.K., S.-F.H. and E.W.-G.D. conducted in situ PL and GIWAXS measurements. L.W. and W.Y. performed thermal simulation. Z.S., R.L. and Z.J. conducted NMR measurement, ESP and DFT calculations. X.G., H.L., Z.D., J.C., Y.-D.W. and X.W. conducted confocal PL, SEM, XPS and KPFM measurements. Q.Z., R.G. and L.-I.D.-B. conducted TRPL and hyperspectral measurements. D.L. and L.K.L. performed tandem device encapsulation. Q.Z. and R.G. wrote the original manuscript. Q.Z., R.G., S.L., N.L. and Y.H. reviewed and edited the paper. All authors read and commented on the paper.

Competing interests

Y.H. is the founder of Singfilm Solar, a company commercializing perovskite photovoltaics. M.X., J.W., X.Z., J.Y. and H.J are employees of Zhejiang Jinko Solar Co. Ltd. L.-I.D.-B. is an employee of Photon etc. Ltd. The other authors declare no competing interests.

Additional information

Supplementary information The online version contains supplementary material available at https://doi.org/10.1038/s41560-026-02010-z.

Correspondence and requests for materials should be addressed to Xinyu Zhang or Yi Hou.

Peer review information *Nature Energy* thanks Eike Koehnenand, Lars Korte, Sang Il Seok and the other, anonymous, reviewer(s) for their contribution to the peer review of this work.

[1]Department of Chemical and Biomolecular Engineering, National University of Singapore, Singapore, Singapore. [2]Solar Energy Research Institute of Singapore, National University of Singapore, Singapore, Singapore. [3]School of Physics, University of Electronic Science and Technology of China, Chengdu, China. [4]Zhejiang Jinko Solar Co. Ltd., Jiaxing, China. [5]Zhejiang Key Laboratory of Advanced Tandem Photovoltaic Technology, Jiaxing, China. [6]Shanghai Jinko Green Energy Enterprise Management Co. Ltd., Shanghai, China. [7]School of Physical Science and Technology, ShanghaiTech University, Shanghai, China. [8]Department of Mechanical Engineering, City University of Hong Kong, Hong Kong, China. [9]Photon etc. Ltd, Montreal, Quebec, Canada. [10]Department of Applied Chemistry and Institute of Molecular Science, National Yang Ming Chiao Tung University, Hsinchu, Taiwan. [11]Center for Emergent Functional Matter Science, National Yang Ming Chiao Tung University, Hsinchu, Taiwan. [12]Department of Mechanical Engineering, National University of Singapore, Singapore, Singapore. [13]These authors contributed equally: Qilin Zhou, Renjun Guo, Shunchang Liu, Nengxu Li, Menglei Xu. ✉e-mail: xinyu.zhang@jinkosolar.com; yi.hou@nus.edu.sg

nature research

Corresponding author(s): Yi Hou

Solar Cells Reporting Summary

Nature Research wishes to improve the reproducibility of the work that we publish. This form is intended for publication with all accepted papers reporting the characterization of photovoltaic devices and provides structure for consistency and transparency in reporting. Some list items might not apply to an individual manuscript, but all fields must be completed for clarity.

For further information on Nature Research policies, including our data availability policy, see Authors & Referees.

▸ Experimental design

Please check: are the following details reported in the manuscript?

1. Dimensions

Area of the tested solar cells	☒ Yes ☐ No	0.925 cm2.
Method used to determine the device area	☒ Yes ☐ No	Corresponding masks were used during the test.

2. Current-voltage characterization

Current density-voltage (J-V) plots in both forward and backward direction	☒ Yes ☐ No	We provide J-V plots in both forward and backward direction in Supplementary Fig. 23.
Voltage scan conditions *For instance: scan direction, speed, dwell times*	☒ Yes ☐ No	See details in Method.
Test environment *For instance: characterization temperature, in air or in glove box*	☒ Yes ☐ No	See details in Method.
Protocol for preconditioning of the device before its characterization	☐ Yes ☒ No	No preconditioning condition is used.
Stability of the J-V characteristic *Verified with time evolution of the maximum power point or with the photocurrent at maximum power point; see ref. 7 for details.*	☒ Yes ☐ No	We provided MPPT data in Supplementary Fig. 23.

3. Hysteresis or any other unusual behaviour

Description of the unusual behaviour observed during the characterization	☐ Yes ☒ No	Negligible hysteresis was observed for tandem devices.
Related experimental data	☐ Yes ☒ No	Hysteresis is not relevant to our concept.

4. Efficiency

External quantum efficiency (EQE) or incident photons to current efficiency (IPCE)	☒ Yes ☐ No	We provide EQE data in Supplementary Fig. 21.
A comparison between the integrated response under the standard reference spectrum and the response measure under the simulator	☒ Yes ☐ No	We compare the integrated Jsc with one from JV scan. The difference between the integrated Jsc from EQE and Jsc from JV scan is within 2% in tandem solar cells, which is within accuracy confidence of the measurements.
For tandem solar cells, the bias illumination and bias voltage used for each subcell	☒ Yes ☐ No	See details in Method.

5. Calibration

Light source and reference cell or sensor used for the characterization	☒ Yes ☐ No	See details in Method.
Confirmation that the reference cell was calibrated and certified	☒ Yes ☐ No	Our solar simulator was calibrated by Si reference cell.

Calculation of spectral mismatch between the reference cell and the devices under test	☒ Yes ☐ No	The champion devices were sent to certification, the certified device spectra mismatch factor can be found in Supplementary Fig. 23.

6. Mask/aperture

Size of the mask/aperture used during testing	☒ Yes ☐ No	Optical aperture masks (0.925 cm2) were used.
Variation of the measured short-circuit current density with the mask/aperture area	☐ Yes ☒ No	No significant variations was observed.

7. Performance certification

Identity of the independent certification laboratory that confirmed the photovoltaic performance	☒ Yes ☐ No	We provide independent measurement data in Fig. 4g and Supplementary Fig. 23.
A copy of any certificate(s) *Provide in Supplementary Information*	☒ Yes ☐ No	We provide measurement report in Supplementary Fig. 23.

8. Statistics

Number of solar cells tested	☒ Yes ☐ No	Fourteen tandem solar cells were tested for statisticsal analysis.
Statistical analysis of the device performance	☒ Yes ☐ No	We provide statistics in Fig. 4 and Supplementary Fig. 20.

9. Long-term stability analysis

Type of analysis, bias conditions and environmental conditions *For instance: illumination type, temperature, atmosphere humidity, encapsulation method, preconditioning temperature*	☒ Yes ☐ No	We provided stability data in Fig. 4h